RSC Advances

PAPER

View Article Online
View Journal | View Issue

Cite this: *RSC Adv.*, 2025, **15**, 42432

Magnetically guided Bi_2S_3@C/Fe_3O_4 nanoparticles for enhanced photothermal-radiation synergy in glioblastoma treatment

Baowang Miao,†[ac] Guidong Zhu,†[a] Shimin Lin,[a] Chi Zhang,[a] Yuze Wang,[a] Dongxun Chen,*[b] Yanjie Liang*[b] and Chengwei Wang*[a]

Received 25th July 2025
Accepted 6th October 2025

DOI: 10.1039/d5ra05381a

rsc.li/rsc-advances

Photothermal therapy (PTT) is limited by its shallow penetration depth, whereas high-dose radiotherapy (RT) can cause significant side-effects. To address these limitations, synergistic therapies integrating RT with PTT have been proposed and investigated as promising treatment strategies. In this study, multifunctional, magnetic-targeting nanoparticles that exhibit high near-infrared absorption and strong photon attenuation were successfully synthesized for the synergistic PTT-RT treatment of glioma. The platform consists of a Bi_2S_3 core encapsulated within a carbon shell. The nanoparticles were further doped with Fe_3O_4 to ensure arrival at the tumor site at an effective concentration to achieve optimal therapeutic outcomes, and to enable preferential aggregation at the intracranial tumor site under the guidance of an external magnetic field. The Bi_2S_3@C/Fe_3O_4 nanoparticles showed high biosafety and a significant synergistic therapeutic effect in combined RT and PTT, both *in vitro* and *in vivo*. The feasibility of Bi_2S_3@C/Fe_3O_4 nanoparticles for glioma treatment was systematically evaluated, providing evidence of the applicability of Bi-based nanomaterials in photothermal radiotherapy.

Introduction

Nanomaterial-based photothermal therapy (PTT) has emerged as a promising approach for tumor treatment, enabling the destruction of tumor cells through thermal ablation, while circumventing challenges such as biological heterogeneity, conventional drug resistance, and potential adverse effects on surrounding healthy tissues.[1] By meticulously controlling parameters such as the intensity of the light source (*e.g.*, 808 nm near-infrared laser), irradiation duration, concentration of the photothermal material, particle dimensions, and surface modifications, precise ablation of tumor tissue can be achieved.[2] However, the limited tissue-penetration depth of laser light (typically <5 mm in biological tissues) often hinders the eradication of deep-seated cancer cells, restricting PTT's application to advanced or infiltrative tumor types.

Radiotherapy (RT), the cornerstone of modern oncology, utilizes high-energy particles to target malignant tumors and induces direct damage to DNA or indirect oxidative stress in cancer cells. Approximately 70% of cancer patients receive RT during their treatment course, underscoring its clinical significance.[3] Nevertheless, the maximum tolerable RT dose is constrained by the sensitivity of the surrounding healthy tissues (*e.g.*, brain parenchyma), precluding complete tumor eradication through dose escalation alone. Enhancing the radiosensitivity of tumors has become a focal research area for addressing this issue. High-atomic-number (Z) elements such as gold, platinum, lead, and bismuth have been extensively investigated as nanoscale radiosensitizers because of their potent photon-attenuating properties, which enhance radiation-induced ionization.[4,5] Nanoparticles composed of these materials have shown promise for improving the efficacy of radiotherapy, with studies demonstrating enhanced cytotoxicity to tumor cells.[6,7] The favorable toxicity profile, cost-effectiveness, high X-ray attenuation coefficient (13.2 $cm^2\ g^{-1}$ at 80 keV), and substantial near-infrared (NIR) absorption of bismuth-based nanomaterials have led to their distinction, with extensive preclinical studies validating their efficacy in various tumor models.[8] However, aggressive tumors such as glioblastoma (GBM) often exhibit intrinsic RT resistance,[9–11] with most recurrences occurring within the original irradiated volume.[12] Hypoxic tumor microenvironments further exacerbate this resistance by reducing radiation-induced DNA damage.[13,14]

Combined PTT-RT therapies offer a synergistic solution for overcoming these limitations.[15,16] PTT not only induces the necrosis or apoptosis of cancer cells *via* hyperthermia (typically >42 °C) but also remodels the tumor microenvironment to enhance oxygenation, thereby reducing the resistance to RT.[17–21]

[a]*Department of Neurosurgery, The Second Qilu Hospital of Shandong University, Jinan, People's Republic of China. E-mail: wangchengwei@sdu.edu.cn*

[b]*Key Laboratory for Liquid-Solid Structure Evolution and Processing of Materials, Ministry of Education, Shandong University, Jinan, 250031, People's Republic of China. E-mail: dongxun_chen@163.com; yanjie.Liang@sdu.edu.cn*

[c]*Department of Neurosurgery, Yiyuan County People's Hospital, Zibo, 256100, People's Republic of China*

† These authors contributed equally to this work.

Conversely, The deep tissue-penetration of RT complements the shallow reach of PTT, enabling comprehensive coverage of both superficial and deep-seated tumor foci. Preclinical studies have consistently shown that the synergistic effect of RT-PTT surpasses that of monotherapy, with the combined treatment achieving higher tumor regression rates.[22–25]

Drug delivery to the central nervous system remains a significant challenge because of the blood–brain barrier (BBB) and unique tumor microenvironment. Nanomaterials with diameters <100 nm can traverse a compromised BBB in mid-late stage GBM, where achieving therapeutic concentrations at the tumor site requires efficient targeting.[26–28] The unique physical properties of magnetic nanoparticles have been leveraged in developing promising platforms for guided drug delivery, allowing external magnetic field-mediated accumulation at target sites.[29]

In this study, an integrated Bi_2S_3@C/Fe_3O_4 nanoplatform was designed for synergistic PTT-RT. The Bi_2S_3 core enables efficient NIR photothermal conversion (37.4% efficiency) and X-ray attenuation, the carbon shell enhances the colloidal stability and biocompatibility, and Fe_3O_4 doping allows magnetic targeting. Using 3D printing, a customized magnetic helmet for nude mice was fabricated to generate localized magnetic fields, guiding preferential accumulation of the Bi_2S_3@C/Fe_3O_4 nanoparticles at intracranial tumor sites. *In vitro* and *in vivo* experiments demonstrate that this platform enhances the efficacy of combined PTT-RT against GBM, offering a novel approach for synergistic neuro-oncology therapy (Scheme 1).

Experimental

Materials

Ammonium bismuth citrate ($C_6H_{10}BiNO_8$, Bi 48–52%) was purchased from Alfa Aesar. Thioacetamide (C_2H_5NS, >99% purity) was purchased from Acros Organics. Polyvinylpyrrolidone (PVP, average $M_w \approx 40\,000$) was obtained from Sigma-Aldrich. 3-Aminophenol (3-AP, 99%) and $FeSO_4 \cdot 7H_2O$ (99.95%) were acquired from Aladdin Reagents. Ammonium hydroxide ($NH_3 \cdot H_2O$, 25–28 wt%) was purchased from Sinopharm Chemical Reagents. Formaldehyde (37%, stabilized with methanol) was provided by Macklin. Acetone (AR) was obtained from Sigma Aldrich. All commercial chemical reagents were directly used for sample preparation without further purification.

Synthesis of Bi_2S_3 NPs

In a typical procedure, 1 mmol of ammonium bismuth citrate and PVP (0.3 g) were loaded into a blue-capped bottle containing 30 mL of pure water. The mixture was heated in a water-bath at 90 °C for 10–15 min to prepare solution A. Simultaneously, 1.5 mmol of thioacetamide was dispersed in 30 mL of pure water and heated in a water-bath at 90 °C for 5–10 min until completely dissolved, forming solution B. Solution B was then slowly added to solution A, and the bottle was sealed. The mixture was heated in a water-bath at 90 °C for 2 h. Bi_2S_3 NPs were obtained by centrifugation and washed with deionized water and anhydrous ethanol.

Synthesis of yolk–shell structured Bi_2S_3@C NPs

In a modified procedure,[30] the prepared Bi_2S_3 NPs and 3-AP (0.8 g) were added to 240 mL of deionized water and ultrasonicated for 5 min. Ammonium hydroxide (0.8 mL) was added as a catalyst and magnetically stirred at room temperature for 30 min. Formaldehyde solution (0.8 mL) was then added and stirring was continued for another 30 min. Thereafter, acetone (160 mL) was added to the solution, and stirring was continued for another 30 min to remove the interior of the material, which was then

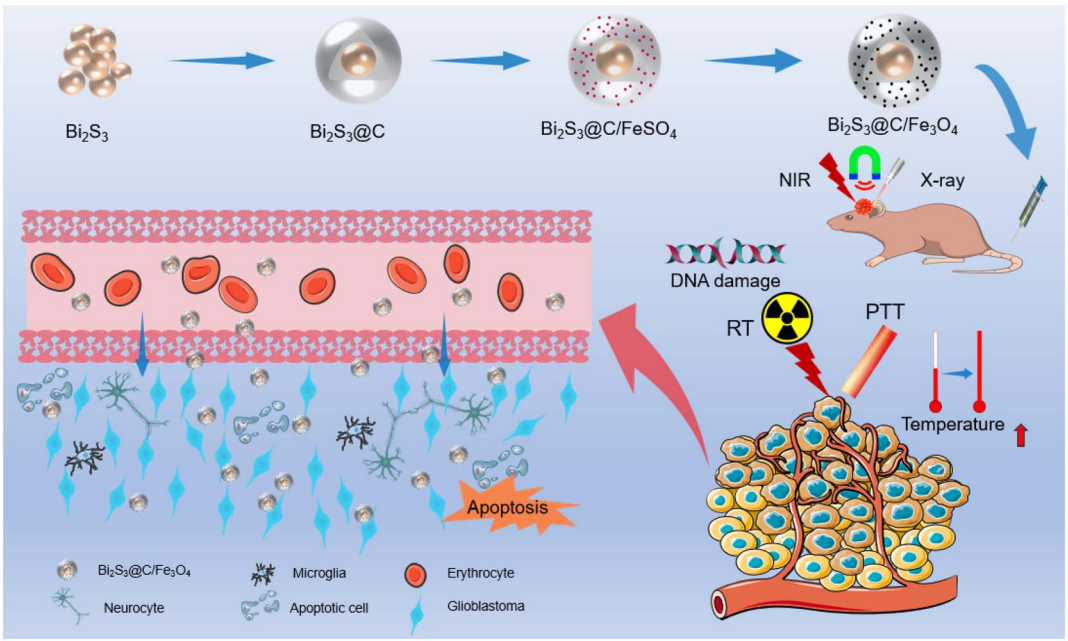

Scheme 1 Preparation of Bi_2S_3@C/Fe_3O_4 and its application in combined PTT-RT for the synergistic treatment of glioma.

collected by centrifugation. The yolk–shell structured Bi_2S_3@C NPs were obtained by centrifugation, washed with water and ethanol several times, and then dried at 60 °C for 12 h.

Synthesis of yolk–shell structured Bi_2S_3@C/Fe_3O_4 NPs

The Bi_2S_3@C NPs (200 mg) were added to a 25 mL single-neck flask and a vacuum (−0.1 MPa) was applied to the sample for 10 min using a vacuum filtration device. Subsequently, 10 mL of $FeSO_4$ solution (0.5 M) was injected into the flask and shaken for 5 min. The solution was restored to atmospheric pressure and the excess liquid was removed. The product was dried at 60 °C for 12 h, followed by sintering in a tube-furnace at 350 °C under argon atmosphere for 4 h to obtain yolk–shell structured Bi_2S_3@C/Fe_3O_4 NPs.

Characterization

The morphologies of the samples were analyzed by field-emission scanning electron microscopy (SEM, JSM-7800F, JEOL). Low- and high-resolution transmission electron microscopy (TEM) data were acquired using a JEOL JEM-2100 instrument with a field-emission gun operating at 200 kV. The crystal structure and phase composition were measured by powder X-ray diffraction (XRD, DMAX-2500PC, Rigaku) at a scanning speed of 10° min^{-1}. X-ray photoelectron spectroscopy (XPS) data were acquired using a Shimadzu AXIS SUPRA spectrometer. Fourier-transform infrared (FT-IR) spectroscopy was performed using an IS50 spectrometer *via* the KBr pellet technique. The zeta potentials were measured using a Malvern Nano ZSE instrument. The absorption spectra were collected using a UV-visible spectrophotometer (UV-vis, SPECORD 200 PLUS, Analytik Jena). The magnetic properties of the materials were examined using a vibrating sample magnetometer (VSM, Lakeshore 7404). An APSP surface area and porosity analyzer (Micromeritics) was used to investigate the specific surface area and pore size distribution of the samples. The temperature of the samples and mice was recorded using an FLIR A310 thermal camera, with a near-infrared laser (808 nm, LSR808N-3W-FC, Ningbo Yuanming Laser Technology Co., Ltd) as the irradiation source.

Analysis of photothermal performance

To evaluate the photothermal performance of the Bi_2S_3@C/Fe_3O_4 NPs, 1.5 mL of the nanosphere dispersion was injected into a quartz tube (10 mm). An 808 nm laser was positioned 10 cm in front of one side of the quartz tube for irradiation. During irradiation, the temperature of the system was monitored every 10 s using a thermal camera placed 50 cm away from the opposite side of the quartz tube, oriented at a 90° to the irradiated side. Notably, to ensure accurate temperature measurements, a layer of 3 M tape (thickness: 0.18 mm, emissivity: 0.95) was adhered to the tested surface of the quartz tube.

In vitro cell cytotoxicity assay

U87MG-Luc and U251 cells were seeded into 96-well plates at a density of 5000 cells per well. Dulbecco's Modified Eagle Medium (DMEM, Gibco, USA) supplemented with 10% fetal bovine serum and 1% penicillin–streptomycin solution was used as the culture medium. The incubation conditions were set to 37 °C and 5% CO_2. Subsequently, various concentrations of NPs were added, and the cells were incubated for 24 h. The final concentrations of the NPs in the medium were 0, 0.1, 0.3, 0.5, 0.7, and 0.9 mg mL^{-1}, and the control group received an equivalent volume of phosphate-buffered saline (PBS). The cell viability was assessed using a Cell Counting Kit-8 (CCK-8).

Cellular uptake assay

U87MG-Luc cells were cultured in 100 × 15 mm cell culture dishes for 24 h to ensure cell adhesion. Subsequently, the cells were co-cultured with the NPs at a concentration of 0.5 mg mL^{-1} for 6 h. After co-culturing, the cells were trypsinized, collected by centrifugation, and fixed in 2.5% glutaraldehyde. The precipitate was washed three times with 0.1 M phosphate buffer (pH 7.4) and pre-embedded. The samples were fixed with 1% osmium tetroxide at room temperature and dehydrated using a graded ethanol series. Finally, the samples were embedded in a resin. Ultrathin sections (60–80 nm) were prepared using an ultramicrotome (Leica UC7, Germany) and mounted on 150-mesh copper grids. Sections were double-stained with 2% uranyl acetate in saturated alcohol and 2.6% lead citrate. The prepared samples were observed and imaged using transmission electron microscopy (TEM; HT7800, Hitachi, Japan).

Synergistic therapeutic effect *in vitro*

Approximately 5 × 10^3 U87MG-Luc cells per well were seeded into 96-well plates and allowed to adhere for 24 h. The wells were divided into eight groups according to their treatments (NPs: 0.5 mg mL^{-1}; NIR: 808 nm, 1.0 W cm^{-2}, 5 min; RT: 6 Gy): (I) PBS, (II) NPs, (III) NIR, (IV) RT, (V) NIR + RT, (VI) NPs + NIR, (VII) NPs + RT, (VIII) NPs + NIR + RT. Upon completing the treatment, the culture medium was replaced with fresh medium. At 2 h post-treatment, the cell culture plates were centrifuged at 400×*g* for 5 min using a porous centrifuge, and the supernatant was carefully removed. A lactate dehydrogenase (LDH) assay kit (Beyotime, China) was used to measure the total intracellular LDH, and the cell survival rate was calculated.

DNA damage and live/dead staining

U87MG-Luc cells (1.5 × 10^4 cells per well) were seeded into confocal small plates and incubated in the medium containing the NPs (0.5 mg mL^{-1}) for 4 h. Following this, the medium was replaced with fresh medium, and the cells were divided into eight groups according to the treatments. After the treatment was completed and after 2 h of incubation, the DNA damage was assessed using a DNA damage detection kit (Beyotime, China). The extent of DNA damage was visualized by confocal microscopy of γ-H2AX foci. Subsequently, the different treatment groups were imaged using a confocal microscope (Carl Zeiss, Germany). Live and dead cells were stained using a calcein-AM/Propidium Iodide (PI) kit (Beyotime, China) and imaged.

Establishment of tumor-bearing model

All animal experiments were approved by the Institutional Animal Care and Use Committee of the Second Hospital of Shandong University (No. KYLL2024827). Female BALB/c nude mice, aged 4 weeks, were obtained from GemPharmatech LLC (Jiangsu, China) and used for the animal experiments. The xenograft tumor model was established by injecting 1×10^6 U87MG-Luc cells (5 μL) into the right brain of BALB/c mice. The right frontal skull of the mouse was removed to increase the penetration of the 808 laser.

In vivo antitumor experiment

Female BALB/c mice bearing U87MG-Luc tumor xenografts were intravenously injected with Bi_2S_3@C/Fe_3O_4 NPs. The dose of the NPs was 10 mg kg^{-1} body weight. At predetermined time points, *in vivo* fluorescence images were acquired using an *in vivo* imaging system (IVIS; PerkinElmer). When the tumors in the mice reached a specific level of radiance, as determined using a fluorescence imaging device, eight groups, each comprising five mice, were randomly assigned. The selected NPs (10 mg kg^{-1} body weight in 100 μL of PBS) were administered *via* tail-vein injection. After 12 h, the mice were observed. The tumor size was monitored every 7 days using a fluorescence imaging device. Mice exhibiting signs of complications, such as pronounced hunchback posture, apathy, reduced movement or activity, leg dragging, unkempt fur, or significant weight loss, were euthanized by cervical dislocation. Fourteen days later, the mice were perfused, and various organs, including the heart, liver, spleen, lungs, and kidneys, were collected and analyzed.

Results and discussion

Characterization of Bi_2S_3@C/Fe_3O_4

Bi_2S_3@C/Fe_3O_4 NPs were synthesized in accordance with a modified literature method,[30,31] and a series of experiments was performed to characterize the morphology of the NPs at each stage of synthesis. Fig. 1 shows a detailed depiction of the micromorphology, structural composition, and surface properties of the Bi_2S_3, Bi_2S_3@C, Bi_2S_3@C/$FeSO_4$, and Bi_2S_3@C/Fe_3O_4 samples, providing a comprehensive understanding of the synthesis process and mechanism underlying the formation of the Bi_2S_3@C/Fe_3O_4 nanoparticles. Fig. 1a shows the scanning electron microscopy (SEM) images and particle-size distribution histograms. Bi_2S_3 nanoparticles with uniform particle size of approximately 54.37 nm and regular morphology were successfully synthesized using the water-bath method. Using these Bi_2S_3 nanoparticles as templates, Bi_2S_3@C particles were prepared through carbon coating *via* a phenolic reaction, resulting in a significant increase in the particle size to 93.36 nm. This external carbon layer facilitated the subsequent incorporation of iron sources. $FeSO_4$ was introduced through negative-pressure *in situ* crystallization, which further increased the particle size to 98.92 nm. Subsequently, well-defined

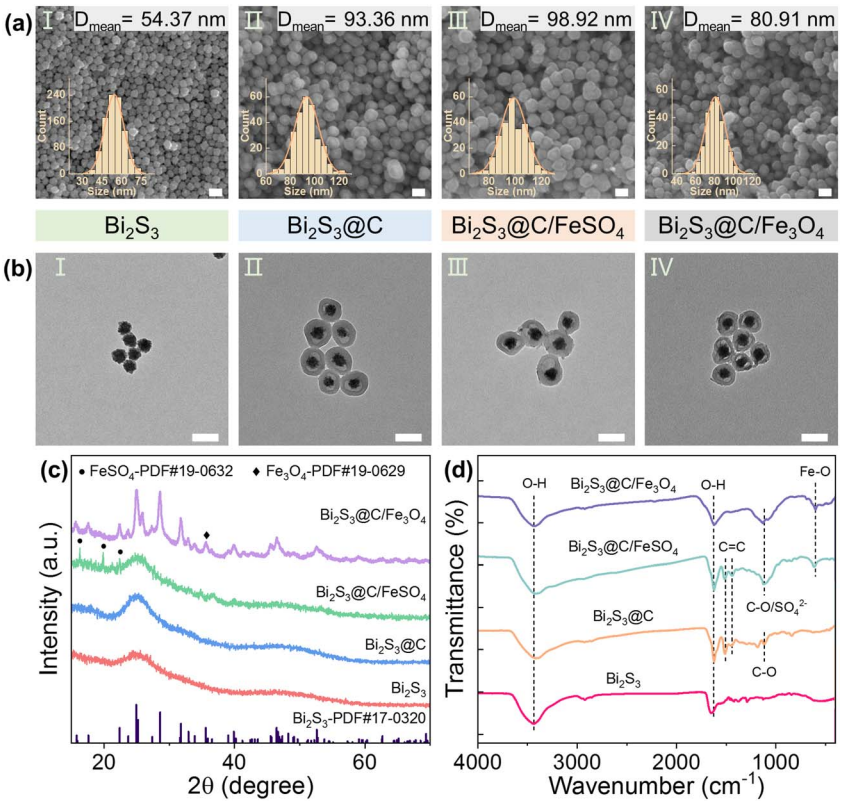

Fig. 1 (a) SEM images (inset: size distributions), (b) TEM images, (c and d) XRD patterns, and FT-IR spectra of Bi_2S_3, Bi_2S_3@C, Bi_2S_3@C/$FeSO_4$, and Bi_2S_3@C/Fe_3O_4 NPs, respectively. Scale bar: 100 nm.

Bi_2S_3@C/Fe_3O_4 nanoparticles with an average diameter of approximately 80.91 nm were synthesized through the *in situ* decomposition and oxidation of $FeSO_4$. The TEM image in Fig. 1b corroborates the microstructural transformations during the synthesis of the Bi_2S_3@C/Fe_3O_4 particles, illustrating the effective dispersion of the Bi_2S_3 precursor core. Following the application of the carbon coating, the development of a yolk–eggshell structure was promoted, thereby creating additional space for the incorporation of iron sources, as depicted in Fig. S2. Ultimately, Bi_2S_3@C/Fe_3O_4 nanoparticles exhibiting a regular morphology, uniform size, and well-dispersed yolk–eggshell structures were successfully synthesized *via in situ* reactions, thus enhancing their potential functionalities. The yolk–shell architecture is particularly advantageous, as the carbon shell not only stabilizes the Bi_2S_3 core against oxidation but also provides a framework for uniform Fe_3O_4 distribution. This structure enhances both the photothermal conversion and magnetic targeting,[32–34] laying the foundation for the synergistic application of these materials in combined therapies. The XRD spectra (Fig. 1c) reveal the crystal structures at various stages of the synthesis process, enabling further clarification of the mechanism of Bi_2S_3@C/Fe_3O_4 synthesis. The FT-IR spectra of the products were acquired at each stage of synthesis for the Bi_2S_3@C/Fe_3O_4 nanoparticles, where the characteristic absorption peaks of different functional groups verified the chemical process and structural evolution of the material. The characteristic peaks changed progressively during the synthesis steps, which perfectly matches the design concept of "core–shell-functional doping." The FT-IR data provide evidence of the photothermal conversion of the chemical structure (Bi_2S_3), magnetic response (Fe_3O_4), and biological adaptability (functional groups of the carbon shell) of the material (Fig. 1d).

The fundamental physical and chemical properties of the synthesized Bi_2S_3@C/Fe_3O_4 nanoparticles were comprehensively characterized, as illustrated in Fig. 2. Fig. 2a shows the energy-dispersive X-ray spectroscopy (EDX) pattern of the Bi_2S_3@C/Fe_3O_4 nanoparticles, where the characteristic peaks

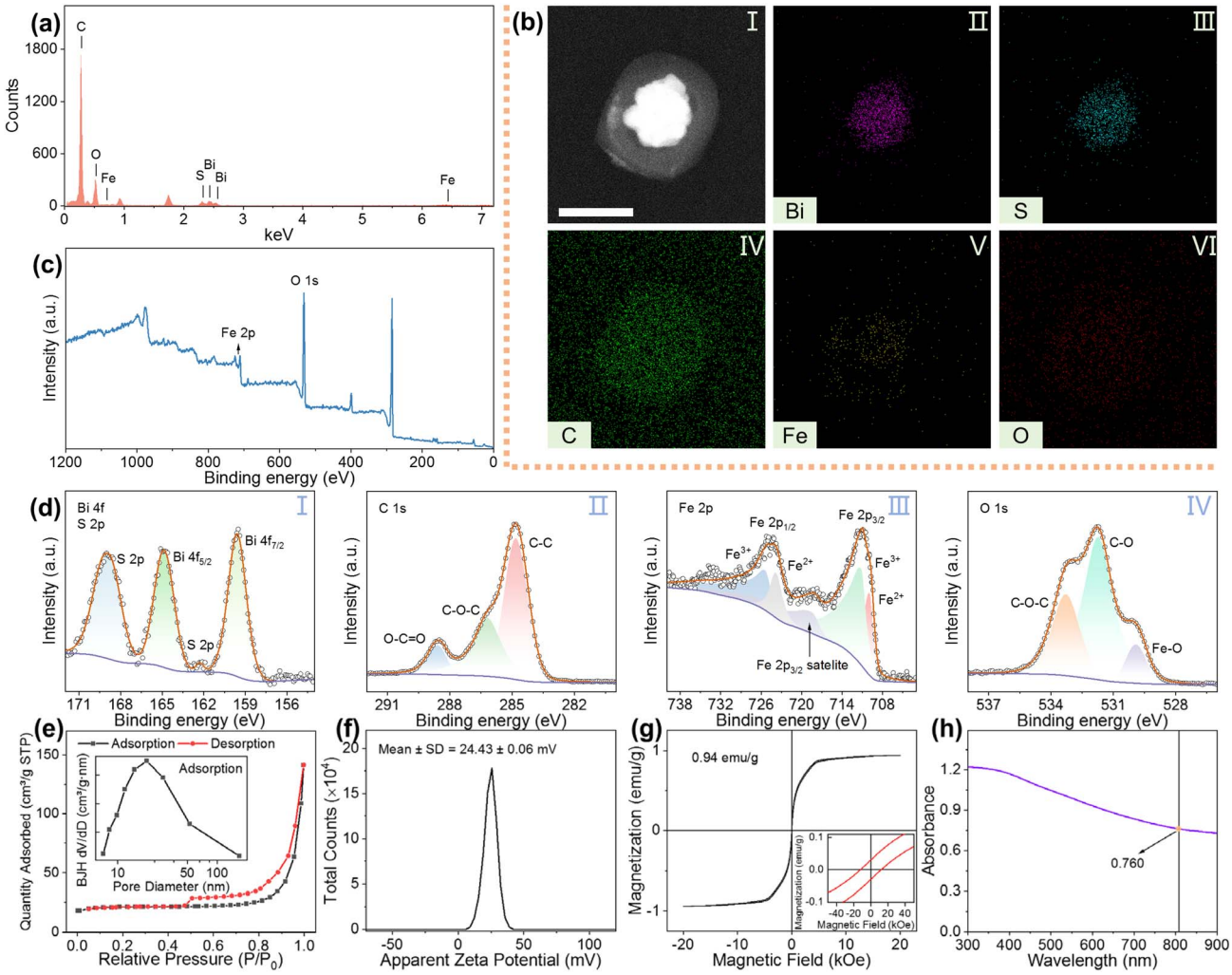

Fig. 2 (a) EDX spectrum, (b) elemental mapping images, (c) and (d) XPS profiles, (e) N_2 adsorption/desorption isotherms (inset: pore-size distribution curves), (f) zeta potential distributions, (g) magnetization loop (inset: zoom-in M–H hysteresis curve), and (h) UV-vis-NIR absorption spectra of Bi_2S_3@C/Fe_3O_4 NPs. Scale bar: 50 nm.

corresponding to Bi, S, Fe, C, and O are clearly discernible. This observation confirmed that the composition of the material was consistent with the anticipated structure. Nonetheless, the Fe peak was less prominent because of the low concentration of Fe and the sensitivity limitations of the instrument. The elemental mapping images (Fig. 2b) further substantiate the uniform distribution of Bi, S, Fe, C, and O throughout the sample, providing preliminary evidence of the successful synthesis of the Bi_2S_3@C/Fe_3O_4 composites. For a more in-depth analysis of the chemical composition and electronic structure, Fig. 2c and d present the XPS data. The presence of Bi_2S_3 was confirmed by the binding-energy peaks of Bi 4f and S 2p (Fig. 2d-I), whereas the C 1s spectrum (Fig. 2d-II) revealed binding-energy signals corresponding to C–C, C–O, and O–C=O groups, indicating the presence of carbon functionalities on the surface of the material. The Fe 2p spectrum (Fig. 2d-III) exhibits characteristic peaks of Fe^{3+} and Fe^{2+}, confirming the formation of the Fe_3O_4 phase. The O 1s spectrum (Fig. 2d-IV) further indicates the presence of C–O, C=O, and Fe–O functional groups, suggesting the occurrence of interactions between the iron oxide and carbon moieties. The nitrogen adsorption–desorption isotherm (Fig. 2e) was classified as a characteristic Type IV curve, indicative of mesoporous properties. The Brunauer–Emmett–Teller (BET) specific surface area was determined to be 81.1073 $m^2 g^{-1}$, with an average pore size of 39.5849 nm, as calculated using the Barrett–Joyner–Halenda (BJH) method (refer to the inset of Fig. 2e). These findings demonstrate that the Bi_2S_3@C/Fe_3O_4 NPs composite features a substantial specific surface area and an optimized pore structure, which significantly enhance its potential efficacy in drug-loading applications. Fig. 2f presents the zeta potential distribution of the Bi_2S_3@C/Fe_3O_4 NPs particles, with an average value of -24.43 ± 0.06 mV, indicating excellent dispersion stability in solution. Dynamic light scattering analysis of the nanoparticles, showing the intensity-weighted hydrodynamic diameter ($D = 172.2 \pm 8.91$ nm) and polydispersity index (PDI $= 0.179 \pm 0.033$), which demonstrates its outstanding dispersibility and stability (Fig. S9). Fig. 2g illustrates the magnetization curve of the Bi_2S_3@C/Fe_3O_4 nanoparticle sample, which demonstrates a saturation magnetization (M_s) of 0.94 emu/g, indicative of significant magnetic-response characteristics. The inset provides an enlarged view of the M–H hysteresis loop, corroborating the superparamagnetic behavior of the material, which is crucial for applications in magnetic separation or targeting. Fig. 2h presents the UV-vis-NIR absorption spectra of the Bi_2S_3@C/Fe_3O_4 nanoparticles, showing broad absorption across the 300–900 nm wavelength range. The absorbance at 808 nm was 0.76, rendering the material highly suitable for photothermal applications.

The ternary structure of "Bi_2S_3 core-carbon shell-Fe_3O_4" was confirmed by EDX/XPS. The advantages of the mesoporous structure and dispersibility were demonstrated by N_2 adsorption and zeta potential measurements. The magnetic response and photothermal potential were verified through analysis of the magnetization hysteresis and UV-vis-NIR spectra, thus completing the logical chain from "structure (core–shell-doping) to performance (magnetism/photothermal property/biological adaptability) to application (synergistic therapy)". This provides a solid materials science basis for *in vitro* and *in vivo* therapeutic experiments.

Photothermal conversion *in vitro*

Photothermal therapy relies on the absorption of near-infrared light; thus, the photothermal properties of the photothermal converter play a critical role in its effectiveness. The photothermal characteristics of the synthesized Bi_2S_3@C/Fe_3O_4 nanoparticles (NPs) were systematically analyzed *in vitro* (Fig. 3).

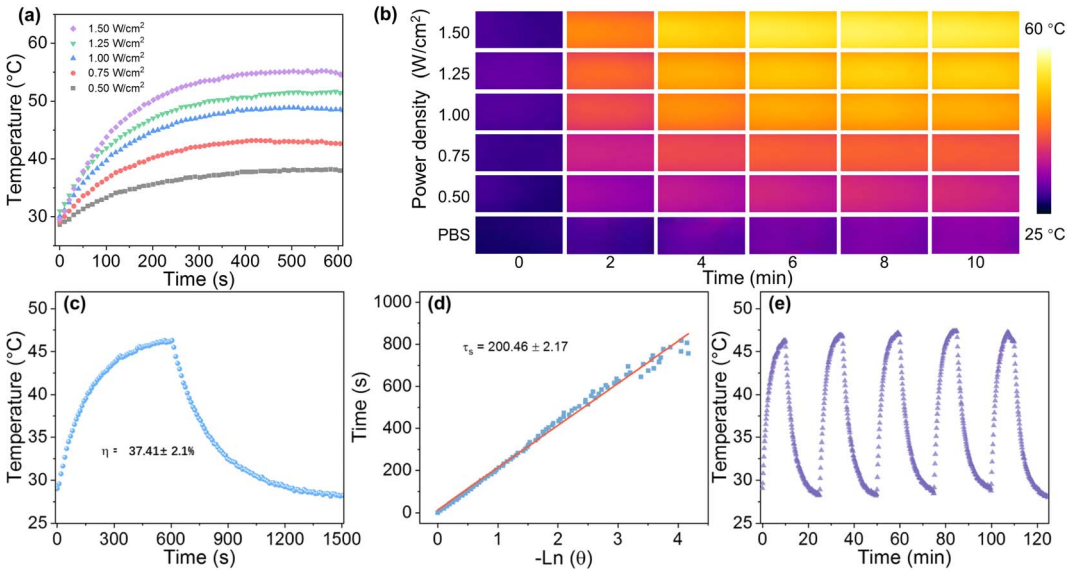

Fig. 3 Bi_2S_3@C/Fe_3O_4 NPs (0.5 mg mL^{-1}): (a) temperature-rise curve with variation of power density (0.5–1.5 W cm^{-2}). (b) Photothermal diagram at different power densities. (c) Photothermal conversion efficiency test (1 W cm^{-2}). (d) Relationship between cooling time and $-\ln \theta$. (e) Cycle stability (1 W cm^{-2}).

Initially, the photothermal effects of the NPs were assessed at a concentration of 0.5 mg mL^{-1} under varying power densities. Fig. 3a illustrates the correlation between the temperature increase and power density. Under 808 nm laser irradiation at power densities ranging from 0.5 to 1.5 W cm^{-2} for 10 min, the temperature of the NPs increased significantly with increasing power density, reaching up to 55.21 °C before gradually stabilizing due to heat dissipation. Simultaneously, an infrared thermal imager was used to record the temperature changes in the solution, providing a more intuitive representation through a two-dimensional color map (Fig. 3b).

By recording a complete heating and cooling cycle (Fig. 3c and d) and utilizing the formula for calculating the photothermal conversion efficiency and absorbance of the NPs at 808 nm, the photothermal conversion efficiency was calculated as 37.41%. To evaluate the photothermal stability of Bi_2S_3@C/Fe_3O_4 NPs, five laser on/off cycling tests were conducted. The results demonstrate no significant changes in the high-temperature performance after five cycles, indicating excellent photothermal stability (Fig. 3e). Collectively, these findings suggest that the Bi_2S_3@C/Fe_3O_4 NPs not only exhibit superior photothermal conversion efficiency and stability but also have considerable potential for tumor cell ablation in photothermal therapy.

Cellular uptake and *in vitro* cytotoxicity

The accumulation of the nanoparticles in tumor cells is crucial for enhancing the antitumor effects. After successfully synthesizing the Bi_2S_3@C/Fe_3O_4 NPs, their cellular uptake and *in vitro* cytotoxicity were systematically investigated. Specifically, U87MG-Luc cells were incubated with the Bi_2S_3@C/Fe_3O_4 NPs at a concentration of 0.5 mg mL^{-1} for 6 h and then imaged by biological TEM for further analysis. The resulting TEM images (Fig. S3) revealed that the Bi_2S_3@C/Fe_3O_4 NPs were significantly internalized in the cells. This successful cellular uptake provides a solid foundation for subsequent *in vitro* and *in vivo* experiments aimed at verifying the therapeutic efficacy of the NPs.

To evaluate the cytotoxicity of the Bi_2S_3@C/Fe_3O_4 NPs, a CCK-8 assay was conducted using U87MG-Luc and U251 cells

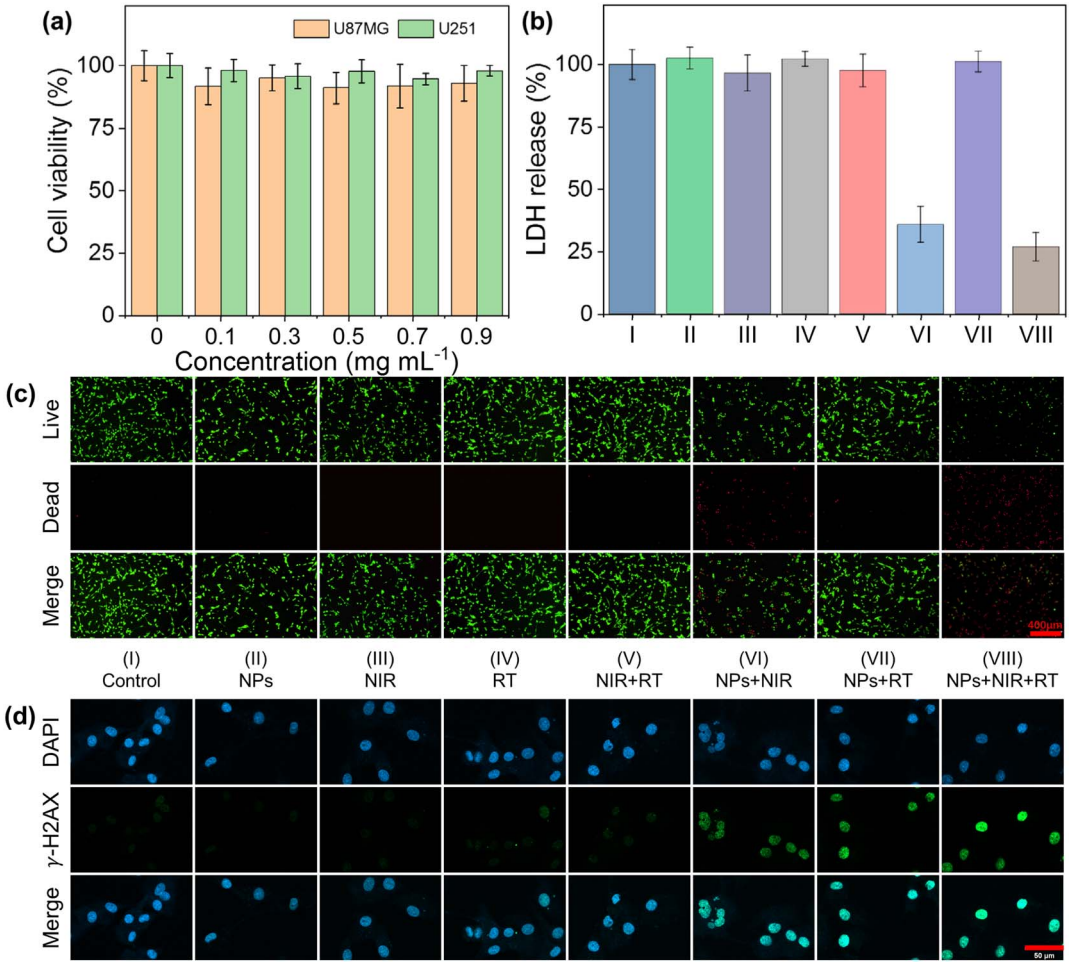

Fig. 4 *In vitro* cellular effects of Bi_2S_3@C/Fe_3O_4: (a) relative viability of U87MG-Luc and U251 cells treated with Bi_2S_3@C/Fe_3O_4 at various concentrations. (b) Release of LDH in U87MG-Luc cells with diverse treatments ($n = 3$; Bi_2S_3@C/Fe_3O_4 0.5 mg mL^{-1}). (c) Results of live/dead staining of U87MG-Luc cells after diverse treatments. Scale bar: 200 μm (d) Qualitative representation of DNA fragmentation with different treatments. Scale bar, 50 μm.

treated with varying concentrations (0, 0.1, 0.3, 0.5, 0.7, and 0.9 mg mL^{-1}) of the NPs for 24 h. The cell viability exhibited a slight concentration-dependent decline (Fig. 4a), indicating that the cytotoxic effect of the NPs increased with concentration. Notably, the cytotoxicity was not significant even at the highest concentration of 0.9 mg mL^{-1}, suggesting that the Bi_2S_3@C/Fe_3O_4 NPs possess excellent biocompatibility and meet the essential requirements for further biomedical applications.

In vitro synergistic therapy

An LDH release assay was conducted to further investigate the effects of photothermal therapy and radiotherapy using a NP concentration of 0.5 mg mL^{-1}. The Bi_2S_3@C/Fe_3O_4 NP group showed significantly reduced cell viability (declining from 96.5% to 35.7%) compared to the control group (Fig. 4b) under NIR treatment alone, as well as under combined RT + NIR treatment (declining from 97.6% to 26.7%). A Live/Dead kit was used to assess the effect of the NPs on U87MG-Luc cells across the eight groups, where living cells were stained green and dead cells were stained red (Fig. 4c). The cell imaging data demonstrated that all cell nuclei in both the NPs + NIR and NPs + NIR + RT groups exhibited strong PI signals associated with chromatin condensation. Notably, the signal was more pronounced in the NPs + NIR + RT group, indicating more extensive cell death compared to that in the other groups, which is consistent with previously reported LDH data. These findings not only illustrate the outstanding photothermal therapeutic efficacy of the Bi_2S_3@C/Fe_3O_4 NPs, but also highlight the synergistic interaction between PTT and RT, thereby reinforcing the considerable potential of the combined techniques for medical applications.

Radiation enhancement is attributed to DNA breakage. Phosphorylated histones H2AX (γ-H2AX) were used to characterize the DNA damage. The control groups exhibited no significant γ-H2AX fluorescence signals (Fig. 4d and S10). Only limited γ-H2AX foci were detected in the RT and NIR + RT groups. In contrast, a significantly higher number of γ-H2AX foci was observed in the NPS + NIR and NPS + RT groups, with the highest number detected in the NPs + NIR + RT group, indicating substantial DNA damage induced by the enhanced X-ray generation in the synergistic treatment. The augmented signal in the NPS + RT group suggests that despite the absence of immediate cell death, as indicated by the LDH and Live/Dead staining assays, the cells sustained significant DNA damage. The strong signal for the NPS + NIR group is attributed to the superior photothermal effect of this treatment, leading to increased cell death. These results suggest that NP-mediated synergistic treatment is an efficient approach for killing U87MG-Luc cells. These findings are consistent and demonstrate the potential of exploiting the sensitization of PT combined with RT for inducing DNA damage in U87MG-Luc cells.

In vivo targeting and synergistic treatment

The distribution and tumor retention of the Bi_2S_3@C/Fe_3O_4 NPs *in vivo* was further evaluated. The fluorescent dye Cy5.5 was successfully loaded into the Bi_2S_3@C/Fe_3O_4 NPs, enabling fluorescence imaging and ensuring stability. To achieve precise localization, 3D printing was used to fabricate a magnetic helmet specifically tailored for nude mice (Fig. S4). Subsequently, the *in vivo* biodistribution and pharmacokinetics of the Cy5.5-labeled Bi_2S_3@C/Fe_3O_4 NPs after intravenous administration were evaluated. As shown in Fig. 5a, the fluorescence

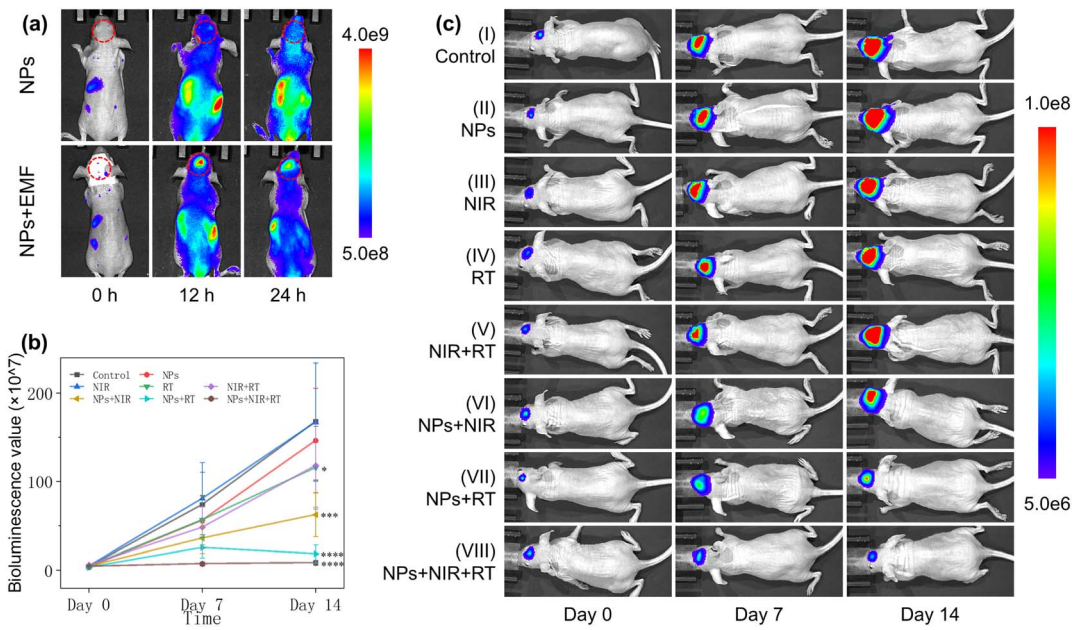

Fig. 5 (a) Fluorescence images of U87MG-Luc tumor-bearing mice intravenously injected with Cy5.5-labeled Bi_2S_3@C/Fe_3O_4 NPs at various time points. (b) Quantification of bioluminescence in tumor-bearing mice. (c) Intracranial GBM growth as determined by bioluminescence analysis of luciferase-expressing U87MG cells monitored on days 0, 7, and 14.

intensity was significantly stronger in the tumors of the nude mice wearing magnetic helmets than in those of the mice without helmets. This result underscores the enhanced tumor accumulation capability of the Bi_2S_3@C/Fe_3O_4 NPs (Fig. S11). Based on these *in vivo* imaging and pharmacokinetic findings, we propose that the optimal time point for irradiation treatment is 12 h post injection. The magnetic helmets address a critical challenge in brain tumor therapy: inefficient drug delivery across the blood–brain barrier (BBB) and consequent inadequate tumor accumulation.[35–37] By leveraging the superparamagnetic properties of Fe_3O_4, the system converts an external physical stimulus (magnetic field) into spatial control over the biodistribution of the NPs.[38–40] This active-targeting modality not only enhances tumor-specific accumulation, but also reduces off-target toxicity, which is a key advantage for central nervous system (CNS) applications where normal tissue sparing is paramount. The optimal 12 h window aligns with the pharmacokinetic profile of mesoporous nanocarriers, ensuring sufficient time for NP extravasation *via* the BBB (compromised in glioma) and subsequent tumor penetration.

Encouraged by the promising *in vitro* results demonstrating the cytotoxicity of the Bi_2S_3@C/Fe_3O_4 NPs to tumor cells, the *in vivo* therapeutic effects of the NPs were further investigated. The *in vivo* therapeutic efficacy of the NPs was evaluated using an orthotopic mouse model of brain glioma (Fig. S5). U87MG-Luc tumor-bearing mice were randomly assigned to eight groups ($n = 5$ per group) and subjected to various treatment regimens. The Changes in the fluorescence intensity within the tumor of the tumor-bearing mice are shown in Fig. 5b and c. The results indicate a significant increase in the intensity of the tumor fluorescence for the control group, whereas tumor growth was effectively inhibited in both the NPs + RT and NPs + NIR groups. Notably, the inhibitory effect was less pronounced in the NPs + NIR group than that in the NPs + RT group; however, the former group still demonstrated slow tumor growth, consistent with the *in vitro* cell experiments. These findings suggest that the NPs enhanced the efficacy of radiation and photothermal therapy *in vivo*. The tumor inhibition effect was most pronounced in the NPs + NIR + RT group. Compared to photothermal therapy and radiotherapy alone, synergistic treatment with the NPs significantly improved therapeutic outcomes in tumor-bearing mice. The orthotopic model recapitulates the clinical challenge of treating deep-seated gliomas, where monotherapies fail owing to radioresistance, PTT depth limitations, and the BBB barrier.[41,42] The Bi_2S_3@C/Fe_3O_4 system addresses these challenges through its multifunctional design. Additionally, H&E staining of major organs from each group revealed that the NPs exhibited low biological toxicity (Fig. S6), with no evident organ toxicity or side-effects observed, while mice in the combined therapy group maintained stable body weight (Fig. S7). The analysis of serum alanine aminotransferase (ALT), aspartate aminotransferase (AST), and blood urea nitrogen (BUN) levels during the treatment process (Fig. S8) showed no abnormal changes. Moreover, mice in the combined therapy group maintained stable body weight (Fig. S7), collectively indicating the high biocompatibility and safety of the Bi_2S_3@C/Fe_3O_4 NPs.This safety profile positions Bi_2S_3@C/Fe_3O_4 as a promising candidate for further preclinical development. The lack of acute toxicity supports the feasibility of repeated dosing, which is a potential requirement for glioma therapy, given its high recurrence rates.[43,44]

In general, the magnetic targeting-photothermal-radiotherapy synergistic strategy proposed in this study provides a new paradigm for GBM treatment, where magnetic targeting enhances NP accumulation in orthotopic gliomas, enabling synergistic RT-PTT *via* radiosensitization while maintaining biocompatibility. These data provide critical insights for translating nanomaterial-based therapies into clinical deployment, specifically demonstrating multimodal efficacy in a clinically relevant glioma model. Future work will focus on optimizing the magnetic field parameters, exploring combinations with immune checkpoint inhibitors, and evaluating long-term recurrence prevention steps toward the clinical translation of this synergistic platform.

Conclusions

In this work, Bi_2S_3@C/Fe_3O_4 NPs were successfully synthesized and their potential for combined RT and PTT applications was evaluated. A wearable magnetic helmet for mice was designed using 3D printing technology, and the nanoparticles achieved local targeting under an external magnetic field. Both *in vitro* and *in vivo* experiments demonstrated that the Bi_2S_3@C/Fe_3O_4 NPs exhibit excellent biocompatibility and superior photothermal and radiotherapeutic properties, significantly enhancing their therapeutic efficacy against GBM. The Bi_2S_3@C/Fe_3O_4 NPs, which integrate photothermal therapy, radiosensitization, and magnetic targeting, represent a promising multifunctional theranostic nanomedicine for GBM treatment and the results provide compelling evidence supporting the application of Bi-based nanomaterials in photothermal radiotherapy.

Author contributions

Baowang Miao: methodology, writing – original draft, visualization, funding acquisition. Guidong Zhu: writing – original draft, conceptualization, funding acquisition. Shimin Lin, Chi Zhang and Yuze Wang: resources, methodology. Dongxun Chen: formal analysis. Yanjie Liang: designed and conceptualized this study. Chengwei Wang: funding acquisition, project administration, review & editing, supervision.

Conflicts of interest

There are no conflicts to declare.

Data availability

The data that support the findings of this study are available from the corresponding author upon reasonable request.

Supplementary information is available. See DOI: **https://doi.org/10.1039/d5ra05381a**.

Acknowledgements

This work was supported by the Key Research and Development Program of Shandong Province (No. 2021CXGC011101), Shandong Province Postdoctoral Innovation Project (No. SDCX-ZG-202303056) and Zibo City Medical and Health Science and Research Projects (20240404046).

Notes and references

1 C. Bastiancich, A. Da Silva and M.-A. Estève, Photothermal therapy for the treatment of glioblastoma: Potential and preclinical challenges, *Front. Oncol.*, 2021, **10**, 610356.
2 G. Y. Yi, M. J. Kim, H. I. Kim, *et al.*, Hyperthermia treatment as a promising anti-cancer strategy: Therapeutic targets, perspective mechanisms and synergistic combinations in experimental approaches, *Antioxidants*, 2022, **11**, 625.
3 Q. Dai, L. Wang, E. Ren, *et al.*, Ruthenium-based metal-organic nanoradiosensitizers enhance radiotherapy by combining ros generation and co gas release, *Angew Chem. Int. Ed. Engl.*, 2022, **61**, e202211674.
4 H. Wang, X. Mu, H. He, *et al.*, Cancer radiosensitizers, *Trends Pharmacol. Sci.*, 2018, **39**, 24–48.
5 M. R. Gill and K. A. Vallis, Transition metal compounds as cancer radiosensitizers, *Chem. Soc. Rev.*, 2019, **48**, 540–557.
6 X. Liu, X. Zhang, M. Zhu, *et al.*, Pegylated au@pt nanodendrites as novel theranostic agents for computed tomography imaging and photothermal/radiation synergistic therapy, *ACS Appl. Mater. Interfaces*, 2017, **9**, 279–285.
7 L. Cheng, S. Shen, S. Shi, *et al.*, Fese(2)-decorated bi(2)se(3) nanosheets fabricated *via* cation exchange for chelator-free (64)cu-labeling and multimodal image-guided photothermal-radiation therapy, *Adv. Funct. Mater.*, 2016, **26**, 2185–2197.
8 J. Deng, S. Xu, W. Hu, *et al.*, Tumor targeted, stealthy and degradable bismuth nanoparticles for enhanced x-ray radiation therapy of breast cancer, *Biomaterials*, 2018, **154**, 24–33.
9 G. Zhu, Z. Sun, Y. Liu, *et al.*, Rational design and organoid-based evaluation of a cocktail car-γδ t cell therapy for heterogeneous glioblastoma, *Adv. Sci.*, 2025, **12**, e2501772.
10 G. Zhu, Q. Zhang, J. Zhang, *et al.*, Targeting tumor-associated antigen: A promising car-t therapeutic strategy for glioblastoma treatment, *Front. Pharmacol*, 2021, **12**, 661606.
11 G. Zhu, J. Zhang, Q. Zhang, *et al.*, Enhancement of cd70-specific car t treatment by ifn-γ released from ohsv-1-infected glioblastoma, *Cancer Immunol. Immunother.*, 2022, **71**, 2433–2448.
12 G. Minniti, D. Amelio, M. Amichetti, *et al.*, Patterns of failure and comparison of different target volume delineations in patients with glioblastoma treated with conformal radiotherapy plus concomitant and adjuvant temozolomide, *Radiother. Oncol.*, 2010, **97**, 377–381.
13 R. Zhou, H. Wang, Y. Yang, *et al.*, Tumor microenvironment-manipulated radiocatalytic sensitizer based on bismuth heteropolytungstate for radiotherapy enhancement, *Biomaterials*, 2019, **189**, 11–22.
14 N. Sadeghi, R. J. Kok, C. Bos, *et al.*, Hyperthermia-triggered release of hypoxic cell radiosensitizers from temperature-sensitive liposomes improves radiotherapy efficacy in vitro, *Nanotechnology*, 2019, **30**, 264001.
15 N. Ma, Y. W. Jiang, X. Zhang, *et al.*, Enhanced radiosensitization of gold nanospikes *via* hyperthermia in combined cancer radiation and photothermal therapy, *ACS Appl. Mater. Interfaces*, 2016, **8**, 28480–28494.
16 S. Anand, T. A. Chan, T. Hasan, *et al.*, Current prospects for treatment of solid tumors *via* photodynamic, photothermal, or ionizing radiation therapies combined with immune checkpoint inhibition (a review), *Pharmaceuticals*, 2021, **14**, 447.
17 A. L. Oei, C. M. van Leeuwen, R. ten Cate, *et al.*, Hyperthermia selectively targets human papillomavirus in cervical tumors *via* p53-dependent apoptosis, *Cancer Res.*, 2015, **75**, 5120–5129.
18 A. Deezagi, S. Manteghi, P. Khosravani, *et al.*, Induced apoptosis by mild hyperthermia occurs *via* telomerase inhibition on the three human myeloid leukemia cell lines: Tf-1, k562, and hl-60, *Leuk. Lymphoma*, 2009, **50**, 1519–1527.
19 G. Speit and P. Schütz, Hyperthermia-induced genotoxic effects in human a549 cells, *Mutat. Res.*, 2013, **747–748**, 1–5.
20 S. Barni, P. Pontiggia, V. Bertone, *et al.*, Hyperthermia-induced cell death by apoptosis in myeloma cells, *Biomed. Pharmacother.*, 2001, **55**, 170–173.
21 T. Ma, Y. Liu, Q. Wu, *et al.*, Correction to quercetin-modified metal-organic frameworks for dual sensitization of radiotherapy in tumor tissues by inhibiting the carbonic anhydrase ix, *ACS Nano*, 2020, **14**, 2553.
22 S. Jiang, Z. Liu, Y. Tian, *et al.*, A comprehensive evaluation of zrc nanoparticle in combined photothermal and radiation therapy for treatment of triple-negative breast cancer, *Front. Oncol.*, 2021, **11**, 801352.
23 M. Yin, X. Chen, Q. Guo, *et al.*, Ultrasmall zirconium carbide nanodots for synergistic photothermal-radiotherapy of glioma, *Nanoscale*, 2022, **14**, 14935–14949.
24 H. Tang, J. Chen, L. H. Qi, *et al.*, Multifunctional aupt nanoparticles for synergistic photothermal and radiation therapy, *Int. J. Nanomed.*, 2023, **18**, 6869–6882.
25 A. Neshasteh-Riz, N. Eyvazzadeh, A. Rostami, *et al.*, Cytogenetic damage from hyperthermia,6 mv x-rays, and topotecan in glioblastoma spheroids, simultaneously, and separately, *J. Cancer Res. Ther.*, 2018, **14**, 1273–1278.
26 T. I. Janjua, P. Rewatkar, A. Ahmed-Cox, *et al.*, Frontiers in the treatment of glioblastoma: Past, present and emerging, *Adv. Drug Deliv. Rev.*, 2021, **171**, 108–138.
27 Z. H. Houston, J. Bunt, K. S. Chen, *et al.*, Understanding the uptake of nanomedicines at different stages of brain cancer using a modular nanocarrier platform and precision bispecific antibodies, *ACS Cent. Sci.*, 2020, **6**, 727–738.
28 Y. Zhou, Q. Liu, H. Cong, *et al.*, Advancements in the management of overactive bladder in women using nano-

botulinum toxin type a: A narrative review, *Curr. Urol.*, 2025, **19**, 77–83.
29 R. Qiao, C. Fu, H. Forgham, *et al.*, Magnetic iron oxide nanoparticles for brain imaging and drug delivery, *Adv. Drug Delivery Rev.*, 2023, **197**, 114822.
30 D. S. Bin, Z. X. Chi, Y. Li, *et al.*, Controlling the compositional chemistry in single nanoparticles for functional hollow carbon nanospheres, *J. Am. Chem. Soc.*, 2017, **139**, 13492–13498.
31 D. Chen, B. Miao, G. Zhu, *et al.*, Controllable synthesis and biomedical applications of bismuth-based nanospheres: Enhanced photothermal therapy and ct imaging efficiency, *Nanoscale*, 2025, **17**, 2281–2291.
32 S. Ma, Y. Zhang, Z. Zhu, *et al.*, Nucleolus-targeting carbon dot nanocomplexes for combined photodynamic/photothermal therapy, *Mol. Pharm.*, 2025, **22**, 958–971.
33 H. Zhang, Y. Li, Z. Pan, *et al.*, Multifunctional nanosystem based on graphene oxide for synergistic multistage tumor-targeting and combined chemo-photothermal therapy, *Mol. Pharm.*, 2019, **16**, 1982–1998.
34 Z. Zhou, Y. Sun, J. Shen, *et al.*, Iron/iron oxide core/shell nanoparticles for magnetic targeting mri and near-infrared photothermal therapy, *Biomaterials*, 2014, **35**, 7470–7478.
35 Y. Jiao, L. Yang, R. Wang, *et al.*, Drug delivery across the blood–brain barrier: A new strategy for the treatment of neurological diseases, *Pharmaceutics*, 2024, **16**, 1611.
36 D. Wu, Q. Chen, X. Chen, *et al.*, The blood–brain barrier: Structure, regulation, and drug delivery, *Signal Transduct. Targeted Ther.*, 2023, **8**, 217.
37 Y. H. Tsou, X. Q. Zhang, H. Zhu, *et al.*, Drug delivery to the brain across the blood–brain barrier using nanomaterials, *Small*, 2017, **13**, 201701921.
38 C. Janko, T. Ratschker, K. Nguyen, *et al.*, Functionalized superparamagnetic iron oxide nanoparticles (spions) as platform for the targeted multimodal tumor therapy, *Front. Oncol.*, 2019, **9**, 59.
39 S. Palanisamy and Y. M. Wang, Superparamagnetic iron oxide nanoparticulate system: Synthesis, targeting, drug delivery and therapy in cancer, *Dalton Trans.*, 2019, **48**, 9490–9515.
40 T. Koyama, M. Shimura, Y. Minemoto, *et al.*, Evaluation of selective tumor detection by clinical magnetic resonance imaging using antibody-conjugated superparamagnetic iron oxide, *J. Contr. Release*, 2012, **159**, 413–418.
41 W. Cheng, H. Qu, J. Yang, *et al.*, Hierarchically engineered self-adaptive nanoplatform guided intuitive and precision interventions for deep-seated glioblastoma, *ACS Nano*, 2025, **19**, 557–579.
42 R. C. Cornelison and J. M. Munson, Perspective on translating biomaterials into glioma therapy: Lessons from *in vitro* models, *Front. Mater.*, 2018, **5**, 27.
43 G. Lai, H. Wu, K. Yang, *et al.*, Progress of nanoparticle drug delivery system for the treatment of glioma, *Front. Bioeng. Biotechnol.*, 2024, **12**, 1403511.
44 K. Scheinemann, U. Bartels, E. Tsangaris, *et al.*, Feasibility and efficacy of repeated chemotherapy for progressive pediatric low-grade gliomas, *Pediatr. Blood Cancer*, 2011, **57**, 84–88.